#1 Transport properties of secondary Dirac fermions

Near the main and secondary NPs, our devices exhibited surprisingly similar carrier mobilities µ (see the main text). They were within a range of ≈20–100×10^3 cm^{2}V^{-1}s^{-1} depending on sample. No short-range resistivity term that often yields a sublinear dependence σ(n) was noticeable in our devices.

As usual for graphene on hBN [S1-S2], near the main NP we find µ to be practically independent of T within our entire T range, which was limited to 150 K to avoid breakdown of the gate dielectric. Near the electron-side secondary NP (eSNP), µ also shows only a weak T dependence. In stark contrast, there is a strong T dependence near the hSNP (Fig. 1a of the main text) such that µ falls below 10,000 cm^{2}V^{-1}s^{-1} at 150K. The behavior did not change significantly below 10 K.

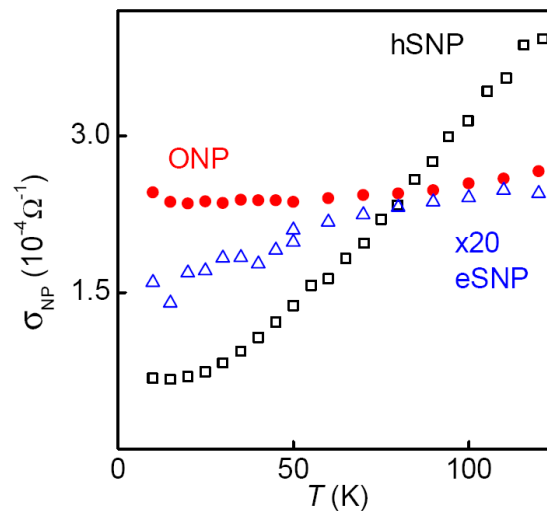

FIG. S1. T dependences of minimum conductivity at the main and secondary NPs. For the electron-side NP, σ$_{NP}$ is scaled by a factor of 20.

Another notable difference between the three NPs is that they exhibit different T dependences of their minimum conductivities σ$_{NP}$ (Fig. S1). For the hSNP, σ$_{NP}$ increases by a factor of 10 between liquid-helium T and 150K. For the eSNP and main NP, changes in σ$_{NP}$ are small (<50%), similar to the standard behavior for graphene with similar µ [S1-S3]. Despite the strong T dependence at the hSNP, it does not follow the activation behavior but evolves linearly with T and then saturates below 20K (Fig. S1). We believe that this dependence is unlikely to be caused by a gap opening or localization effects because we have found σ$_{NP}$ insensitive to small magnetic fields B <0.1T [S4]. Similar σ$_{NP}$(T) were reported for high-µ suspended devices and attributed to a combined effect of thermally excited carriers and T-dependent scattering [S5-S6]. The observed T dependences cast doubt that an hBN substrate can induce large energy gaps envisaged theoretically [S7-S8].

In general, the observed transport properties and, especially, different T behavior for hole- and electron-side Dirac fermions are puzzling and remain to be understood.

#2 Thermal broadening of secondary Dirac points

Another important difference between the main and secondary NPs is their different thermal broadening. At low T, the main DP is broadened by charge inhomogeneity δn, which is $\sim 10^{11}$cm^{-2} in our aligned devices. As expected for such δn [S5-S6], we observe little additional broadening at the main NP with increasing T (Fig. 1a). In contrast, the hSNP becomes strongly and visibly broader with T despite high δn (Figs. 1a and S2). This broadening can be analyzed in terms of the number Δn_T of thermally excited charge carriers [S5-S6]. If δn is relatively small (δn leads to residual broadening at low T), thermal carriers provide a dominant contribution to $\sigma(n)$ at the NPs. Accordingly, the peak in ρ_{xx} becomes lower and broader with increasing T and its top gets rounder. The speed of this broadening as a function of T depends on the density of states (DoS) available for thermal excitations. It was shown theoretically and observed experimentally that Δn_T varies as T^2 and T for the linear and parabolic spectra in graphene and its bilayer, respectively [S5-S6].

We have employed the same procedure as described in detail in ref. S6 to probe the DoS at the secondary DPs in our graphene superlattices. An example of this analysis is shown in Fig. S2 that plots the total number of carriers, $\Delta n_T + \delta n$, at the main and hole-side NPs for device A of the main text. The hSNP broadens >10 times faster than the main NP but both evolve as T^2. Because the peak at the hSNP is large and broadens rapidly, our experimental accuracy is high and the observed square T dependence unequivocally proves that the spectrum near the hSNP is linear, that is, Dirac-like. The eSNP also exhibits rapid thermal broadening but, for the small ρ_{xx}, quantitative analysis is difficult in this case.
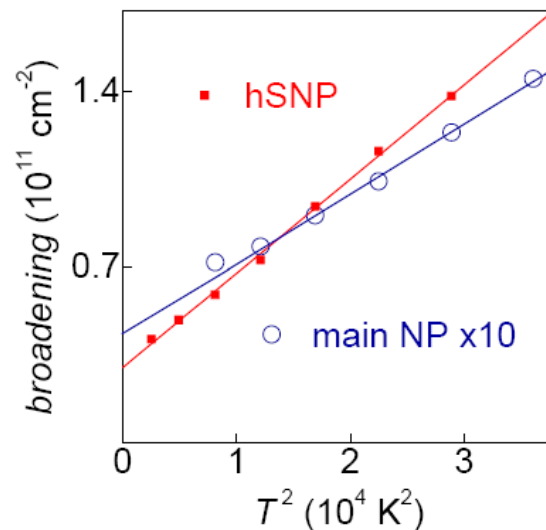

Fig. S2. Number of thermal charge carriers at the main and secondary NPs. The ratio between slopes of the red and blue lines is ≈ 13. The T^2 dependence proves that the spectrum at the new NPs is linear.

For a Dirac spectrum with degeneracy N, Δn_T is proportional to N/v_F^2 [S6]. The average Fermi velocity v_F^S for the secondary Dirac spectra in graphene on hBN was estimated as $\approx 0.5 v_F$ [S9], in agreement with theory [S10-S11]. Therefore, the observed Δn_T ratio of 13±3 (Fig. S2) points at a triple degeneracy for the hole-side secondary DPs, consistent with the models that assume only a scalar potential modulation [S9-S13]. We

also note that the main NP (blue curve) exhibits exactly the same speed $\Delta n_T/T^2$ of thermal broadening as previously reported for the NP in suspended graphene with little δn [S5], which shows good consistency of employing this approach for different graphene systems.

#3 Further examples of Landau fan diagrams

Figure S3 shows another superlattice fan diagram observed in our experiments. The central panel plots the entire diagram whereas the left and right panels zoom-in on the secondary NPs. In the conduction band, the third generation of DPs is seen an oscillatory network emerging beyond the eSNP, similar to the case in Fig. 2b and 3a of the main text. Near the hSNP, individual peaks in ρ_{xx} due to third-generation DPs are not resolved as a function of n and merge into continuous bands, running parallel to the n-axis beyond the hSNP (see Figs. S3a and S4a). These bands can be referred to as Zak oscillations [S14] and are different from both Shubnikov-de Haas and Weiss oscillations.
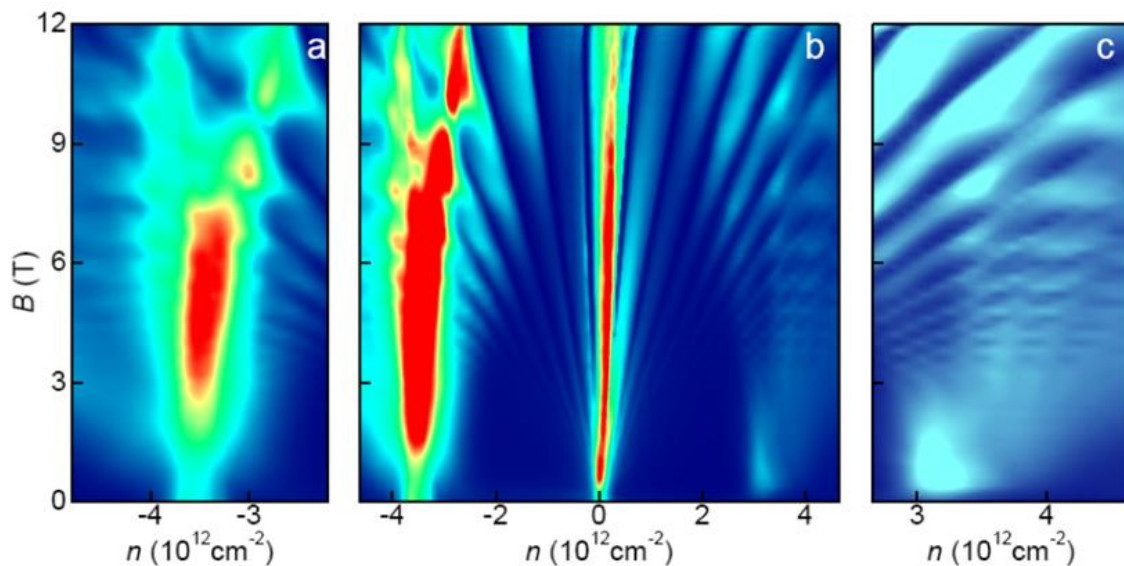

Fig. S3. Landau fan diagrams for device D. **b** – Complete diagrams $\rho_{xx}(n,B)$ showing the main and secondary NPs. **a, c** – Zooming in near the hole- and electron-side DPs, respectively. The blue-to-red scale is from 0 to 16, 8 and 1kOhm for plots a, b and c, respectively. The device exhibits somewhat higher charge inhomogeneity than device A of the main text and, accordingly, the hSNP is broader and its splitting occurs in higher B. The narrow minima in ρ_{xx} along $\nu_S = \pm 2$ (such as in Fig. 2a of the main text) are not seen in this device, although the associated narrow extrema in ρ_{xy} survive the inhomogeneity (see below). The data are taken by sweeping gate voltage at every 0.25T.

In ρ_{xx} measurements, maxima due to third-generation DPs can be difficult to resolve as they often merge into continuous bands for a given B (Fig. S4a). In this case, individual NPs are still seen clearly in Hall measurements. This is illustrated in Fig. S4a-b, which compares fan diagrams for ρ_{xx} and ρ_{xy} for the same range of n and B. The Zak oscillations seen in ρ_{xx} are split into separate spots in ρ_{xy}, similar to the case in Fig. 3a-b of the main text. The white spots in Fig. S4b correspond to deep minima in ρ_{xy} and, near the hSNP, the Hall effect repeatedly changes its sign as a function of B. These minima are accompanied by maxima in ρ_{xx}. Zak oscillations as a function of B are well described by unit fractions of ϕ_0 per superlattice unit cell (Fig.

S4c-d). This behavior is in good agreement with that reported for devices B and C in Fig. 3 of the main text and, in fact, was found in all our devices. For different devices, the observed $1/B$ periodicities varied according to their $S_\otimes$ determined from the same fan diagrams as $S_\otimes = 4n_s^{-1}$ [S11].
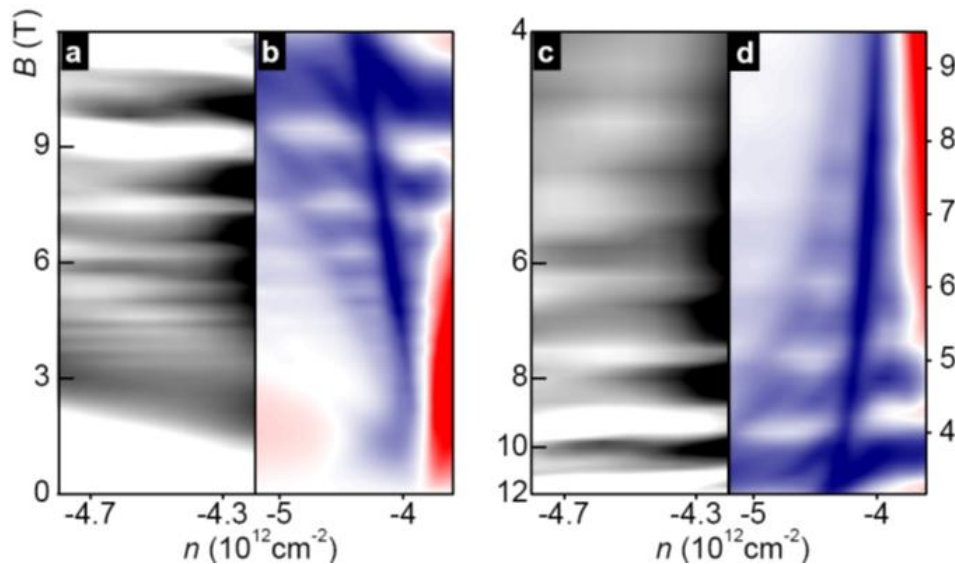

Fig. S4. Zak oscillations. **a** – ρ_{xx} and **b** – ρ_{xy} as a function of n and B beyond the hSNP. Device D as in Fig. S3. Grey scale in (a): 1.5 (white) to 2.8 kOhm (black). Color scale in (b): blue to white to red correspond to -0.2 to 0 to 0.2 kOhm. **c,d** – Same data replotted as a function of $1/B$. The left y-axis is in units of B; the right one in units $\phi_0/B \times S_\otimes$. It is clear that the oscillations are periodic in $1/B$ and correspond to unit fractions of ϕ_0 per superlattice unit cells.
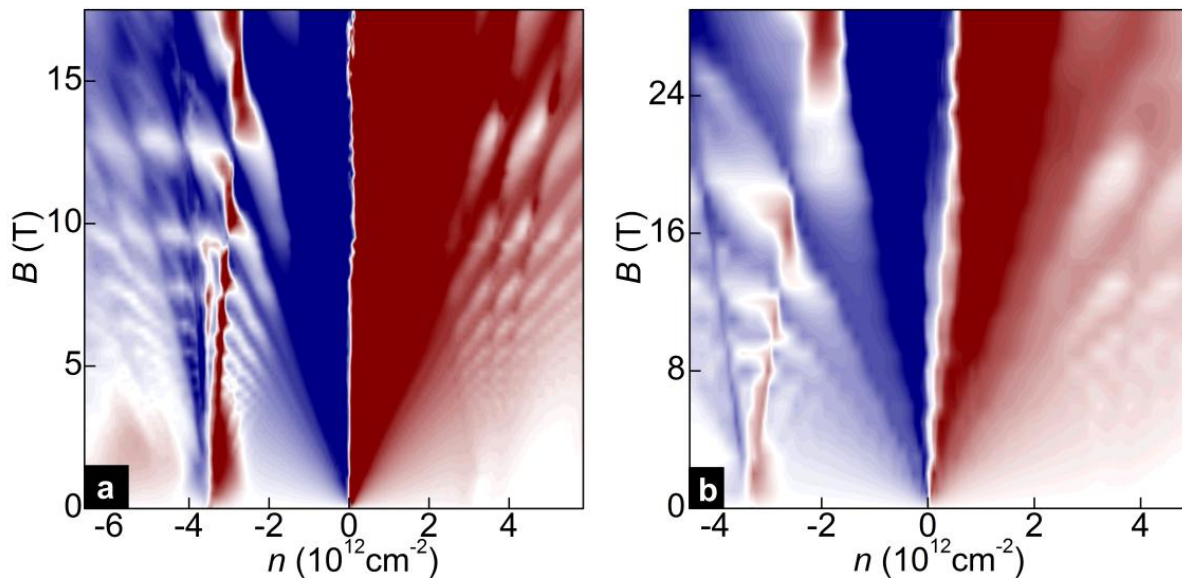

Fig. S5. High-B behavior of ρ_{xy} with numerous third-generation NPs. Scale: blue to white to red corresponds to -2 to 0 to 2 kOhm in (a) for device B and -6 to 0 to 6kOhm in (b) for device C. The data are taken by sweeping gate voltage at every 0.25T in (a) and 1T in (b) (this discreteness leads to the small-scale structure clearly visible at the lower-B parts). The slight shift of the main NP in (b) is specific to this device and probably due to suppression of remnant doping by high B. Note that the oscillations near the eSNP do not lead to the sign change in the Hall effect but ρ_{xy} still reaches very close to zero.

For completeness, Figure S5 shows the full Landau fan diagrams $\rho_{xy}(n,B)$ measured for devices B and C. The data partially appeared in Figs. 3b,e of the main text where the full diagrams were cropped and presented in a scale linear in $1/B$. Fig. S5 again shows repetitive reversals of the Hall effect with increasing B, a phenomenon that has never been observed in other systems.

#4 Superlattice QHE states

With reference to Fig. 2 of the main text, Figure S6 shows the QHE states running along $\nu_S = \pm 2$ at various T in $B = 5T$, just before the central peak at the hSNP splits into two. The minima in ρ_{xx} become deeper with decreasing T (Fig. S6a) but do not reach the zero resistance state even at 1K, being blurred by charge inhomogeneity that suppresses the perfect edge state transport in our relatively narrow devices.
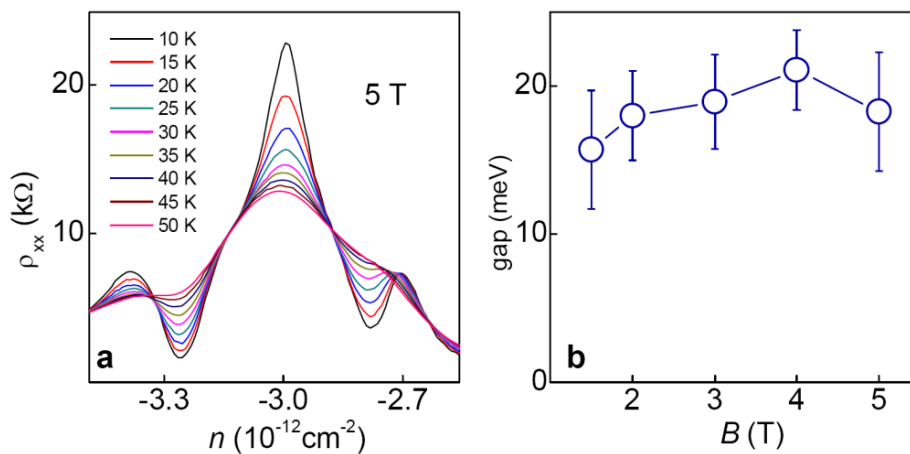

Fig. S6. Quantum Hall effect for secondary Dirac fermions. **a** – T dependence near the hSNP in constant B. **b** – Corresponding energy gaps and their field dependence. The gaps were evaluated by analyzing T dependences such as in (a) by using the Lifshitz-Kosevich formula (see, e.g., ref. [S3]). We did not investigate in detail the T dependence after the central peak split in higher B but, qualitatively, the gaps' size does not change up to 14T (see the T dependence shown in Fig. 2d of the main text).
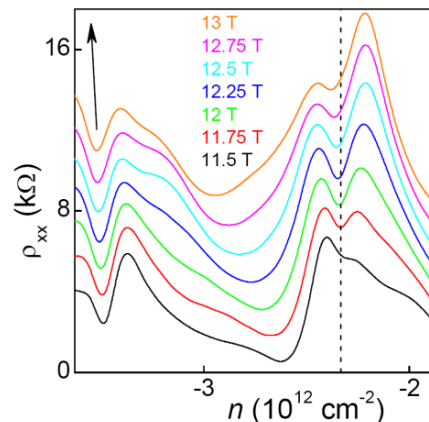

Fig. S7. Detailed evolution of the QHE states emerging near $\nu_S = \pm 2$ as a function of B as they cross the $\nu = -10$ state originating from the main DP (Device A; $T=20K$). The curves are shifted vertically for clarity. The vertical line is to indicate little shift for the right ($\nu_S = +2$) state. The arrow marks a fractal slope $\Delta\nu = -5/3$.

By analyzing T dependences such as in Fig S6a, we have obtained the corresponding gaps in different B (Fig. S6b). Within our experimental accuracy, the gaps for ν_S =-2 and +2 are equal and do not depend much on B (except for B where unit fractions of ϕ_0 pierce the superlattice unit cell), consistent with the fact that the width of the narrow white stripes in Fig. 2a of the main text does not change.

Finally, we want to point out an intriguing behavior of the secondary QHE states running along ν_S =±2 when they 'hybridize' with the QHE states coming from the main NP. This is seen as the step-like waving of the white lines in Fig. 2a of the main text, which change their slopes each time the ν_S =±2 states cross the QHE states originating from the main DP. To examine this behavior further, Fig. S7 shows ρ_{xx} in the interval where the ν_S =±2 states are intersected by the ν =-10 state. One can see that the position of the right minimum changes little with B. The changes (if any) are consistent with a small negative slope $\Delta n/\Delta B$ rather than running parallel to any positive ν_S. The better developed minimum at $n \approx$-3.5×10^{12}cm^{-2} moves leftwards, as expected for this state that shows the general tendency to run along ν_S =-2 (Fig. 2a). However, the speed at which the minimum's position moves with B is lower than ν_S =-2 necessitates. Furthermore, Fig. 2d of the main text shows that, as ρ_{xx} tends to zero, ρ_{xy} develops symmetrically with respect to the Hall plateaus originating from the main NP. We speculate that, if this particular development continues, new QHE plateaus may appear at $h/e^2(1/\nu +1/\nu_S)$ where h/e^2 is the resistance quantum. For the case ν =-10 in Fig. 2d, this would infer ρ_{xy} =-(3/5) and +(2/5)×h/e^2 and correspond to fractional fillings -5/3 and +5/2. To this end, we note that the best developed QHE state (deepest minimum in ρ_{xx}) runs parallel to ν=-5/3 in the corresponding B interval as shown by the arrow in Fig. S7. The overall behavior may indicate that our fractal quantum Hall system supports a single-particle fractional QHE by mixing different integer QHE states.

#5 Spectral characteristics of graphene superlattices

As shown in Refs. S7-S12, there exist 3 principal scenarios for the superlattice spectrum of graphene placed on a hexagonal substrate. All these scenarios lead to secondary DPs at the edges of the lowest-energy moiré minibands in zero B [S11]. However, detailed spectra depend on size and relative strength of the phenomenologically introduced moiré pattern parameters, $u_{0,1,3}$ in the Dirac Hamiltonian for electrons in each of the two graphene valleys ($\varsigma = \pm 1$),

$$H_{moiré} = v_F \vec{p} \cdot \vec{\sigma} + u_0 f_1 + \varsigma u_3 f_2 \sigma_z + \varsigma u_1 (\vec{l}_z \times \nabla f_1) \cdot \vec{\sigma} \qquad (1)$$

where $\sigma_{x,y,z}$ are the Pauli matrices acting on the sublattice components of the electronic wavefunction [(A,B) in the valley K and (B,-A) in K'], $\varsigma = \pm 1$ for K and K' valleys; $f_1 = \sum_{n=0..5} e^{i\vec{b}_n \cdot \vec{r}}$ and $f_2 = \sum_{n=0..5}(-1)^n e^{i\vec{b}_n \cdot \vec{r}}$, where six vectors $\vec{b}_n$ (with $|\vec{b}_n| = b$) are obtained by consecutive 60° rotations; $\vec{b}_n = \hat{R}_{n\pi/3}\vec{G}$ of the reciprocal lattice vector $\vec{G} = [(1 + \delta)\hat{R}_\theta - 1]\vec{b}_G$ of the moiré pattern, and $\vec{b}_G$ and $(1 + \delta)\vec{b}_G$ are the principal reciprocal lattice vectors of aligned graphene and BN lattices, rotated by a small misalignment angle θ.

Three characteristic miniband spectra can be found [S11] for Dirac electrons described by the model in Eq. (1): (a) for small values of parameters $u_{0,1,3}$, strongly overlapping minibands without clearly separated band edges; (b) for particular relations between these parameters (for example, $u_{1,3} = 0$), a triplet of isolated secondary DPs with anisotropic Dirac velocities at the edge of the hexagonal mini Brillouin zone of moiré superlattice; and (c) more generically, one isolated secondary DP at a corner of the mini Brillouin zone (in each graphene valley) in either valence or conduction band, with a second-generation Dirac velocity of $\approx 0.5 v_F$. Except for special choice of moiré superlattice parameters, spectra of the Hamiltonian in Eq. (1) do not have electron-hole symmetry. Examples of the calculated characteristic miniband spectra for each of the three cases can be found in Ref. [S11].

Figures S8-S10 show examples of the magneto-electronic spectra expected for our graphene superlattices. In Fig. S8, we limit the plotted values to fluxes $0.1\phi_0 < \Phi < 0.6\phi_0$, which for our devices corresponds approximately to B between 3 and 20T, that is, our typical experimental range. The calculated data are similar to those presented in Fig. 3c,d of the main text and obtained by using the procedure described in Ref. [S11]. We use 3 exemplary sets of moiré parameters, which are chosen to illustrate possible scenarios for graphene-on-hBN superlattices, taking into account the electron-hole asymmetry with a stronger secondary DP in graphene's valence band. Black dots in Fig. S8 present energies of states at the center of Zak's magnetic minibands found for arbitrary fractional flux values $\Phi = BS_{\otimes} = (2p/q)\phi_0$ [S14-S18]. In Figure S8a, we also show so-called spectral support [S16], that is, the entire miniband for several even and odd values of q (blue intervals; $p = 1$).

In the lower-B part of the plots, one can see remnants of the original Dirac spectrum with its Landau levels (LL) progressively broadened by the superlattice potential. To illustrate this fact, the red curves in Fig. S8a show several original LLs, in the absence of a superlattice potential. The superlattice spectra also contain reminiscence of Dirac-like quantized levels originating from secondary DPs. This is illustrated in Fig. S8a by another set of red curves beginning from $\approx -0.5 v_F b$. These LLs evolve as $-0.51 v_F b \pm 0.5 v_F \sqrt{2N\hbar eB}$ with $N = 0,1$, ... The green dots in Fig. S8a (also, Fig. 3c of the main text) show positions of the Fermi energy for $n = -n_S \equiv -4/S_{\otimes}$, that is, for the complete filling of the first moiré miniband in the valance band. These calculations are done by counting the number of filled magnetic bands (whose capacity and degeneracy depend on p and q [S14-S15]). The reason for us to focus on this particular density is that it corresponds to the half-filled zero LL originating from the secondary DP at the edge of the first moiré miniband in zero B. Therefore, this is the state that exhibits the initial (zero-B) change in the sign of Hall conductivity. Moreover, at Φ where this LL (zero N for the secondary DP) splits into pairs of magnetic minibands, the Fermi level lies in a gap between them, which happens at $\Phi = \phi_0/(q+1/2)$ (for example, $\Phi = 2/3, 2/5$ or $2/7\phi_0$). In this case, we also expect both σ_{xx} to become zero and Hall conductivity to change sign. By counting filled states in magnetic minibands calculated for the flux $\Phi = \phi_0/q$, we find that in the latter case the Fermi level lies in the middle of Zak's magnetic bands and, although we have not find a way to determine the sign of ρ_{xy} in this case, we can

certainly state that Hall conductivity should once again change its sign and, therefore, take zero value somewhere in between two consecutive values of $\Phi = \phi_0/(q +1/2)$.
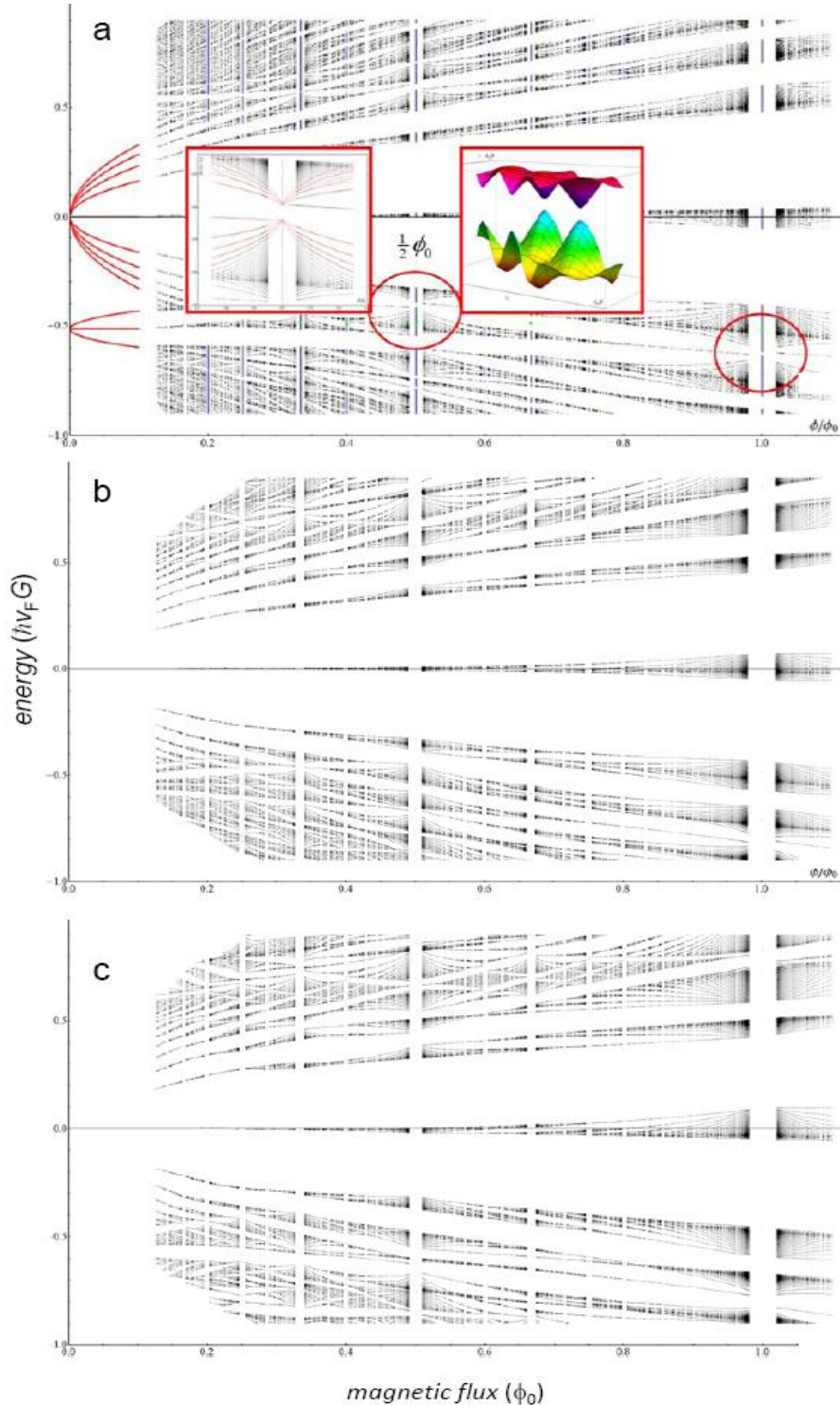

Fig. S8. Moiré butterflies spectra for characteristic superlattice potentials [S11]. **a** − u_0 = -0.031, u_1 = -0.015, u_3 = 0.054; **b** − u_0 = -0.072, u_1 = u_3 = 0.014 and **c** − u_0 = -0.1, u_1= u_3 = 0 where u are in units of $v_F b$. The energy scale is such that the secondary DPs appear at ±1/2. The right inset in (a) shows the energy dispersion (Zak's minibands [S14]) found in the energy range around the secondary DP for ϕ_0/Φ =2; the left inset demonstrates that Zak's minibands are associated with a gapped Dirac-like spectrum and exhibit LLs characteristic of Dirac fermions (also, see ref. S11).

Furthermore, Fig. S8 shows that the zero-N LL is robust and the superlattice potential broadens it relatively weakly over the entire range of Φ for this figure. This level is isolated from the rest of the Hofstadter spectrum by the large cyclotron gap E_1. For our superlattice modulation of ~50meV [S9], the $N = \pm 1$ LLs are also reasonably well isolated. In contrast, LLs with higher N strongly overlap, especially at concentrations near and above the secondary DPs. Therefore, graphene superlattices in quantizing B of several tesla are typically in the regime of strong coupling [S19-S20]. Only for $\Phi > \phi_0$, the superlattices are expected to enter again in the regime of weak coupling where individual LLs are well isolated from each other, and the superlattice potential results in an internal structure within each Landau band [S19-S21]. It would require B >30T to access this regime experimentally. For completeness, the corresponding spectra expected in such B are shown in Fig. S9.
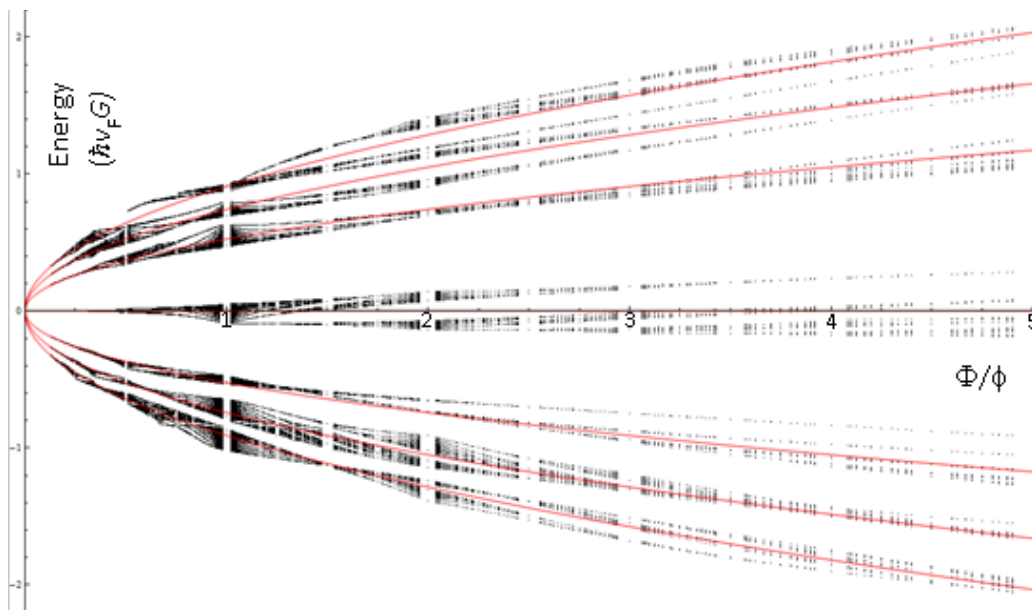

Fig. S9. Moiré butterfly for graphene superlattice in ultra-high B. Only the first LLs with $|N| \leq 3$ are shown. Superlattice potential V =60meV, that corresponds to u_0 = -0.1; $u_1 = u_3 = 0$. The original LLs (zero V) are shown in red. Black dots mark the superlattice states as in Fig. S8. The fractal structure with individual LLs (Hofstadter's butterfly) was previously studied for semiconductor superlattices in refs. [S19-S20]. An intra-LL structure is also noticeable in our Fig. 3a-b. However, the spectrum becomes particularly rich in the regime of strong coupling where the bands originating from different LLs overlap (Fig. S8). In our case, this condition is met for $\Phi < \phi_0$, that is, in B <30T.

The most striking feature of our moiré butterflies is self-similar sets of LLs that resemble those for Dirac fermions and repetitively appear over the entire superlattice spectrum (two circles in Fig. S8a point at characteristic regions). To understand the origin of these local quantized spectra, we have analyzed the miniband dispersion at fractional flux values ϕ_0/q and found that edges between pairs of consecutive minibands systematically display spectra $\omega_N \pm (u^2k^2 + \Delta^2)^{1/2}$, that is, correspond to gapped Dirac fermions. One such dispersion is shown as an inset in Fig. S8a.

If we treat $\delta B = (B - B_q)$ as an effective magnetic field acting on electrons in Zak's magnetic minibands that appear at $B_q = (1/q)\phi_0/S_\otimes$ [S14], the gapped Dirac fermions give rise to a Landau-level fan with $E_{N=1,2,\ldots} = \varepsilon_N \pm \sqrt{Nu^2 e|\delta B| + \Delta^2}$ and $E_0 = \varepsilon_q + \Delta\, sign(\delta B)$. Using $\varepsilon_q(B) \approx \omega_N + c\delta B$ which takes into account an overall average shift of the parent Landau level, we have computed the corresponding spectrum and plotted it in the second inset in Fig. S8a (also, see Fig. 3d of the main text).

Finally, we replot one of our moiré butterflies (Fig. S8a) as a function of ϕ_0/Φ (that is, $1/B$) and the energy renormalized to the energy E_1 of the 1st LL in the main spectrum. This is shown in Fig. S10 and allows easier comparison with the corresponding experimental plots in Figs. 3b,3e,S4c-d. The internal structure of LLs also becomes clearer in this presentation. One can see that the fractal spectra are different from the Hofstadter butterfly described by Harper's equation [S16] as well as from the moiré butterfly expected in twisted graphene bilayers [S17]. Moreover, there is no recurrence of the same fractal pattern within each Landau band. Such repetition of the Hofstadter butterfly is characteristic of semiconductor superlattices where a perfect periodicity within isolated Landau bands is expected for each unit between $\phi_0/\Phi = q$ and $q+1$ [S19-S21]. In our case, we notice a different periodicity: q-th unit of N-th Landau level closely resembles $(q+1)$-th unit for $(N+1)$-th LL (see Fig. S10). Further work is required to understand fractality and properties of the intra-LL structure in graphene superlattices even in the limit of weak coupling.
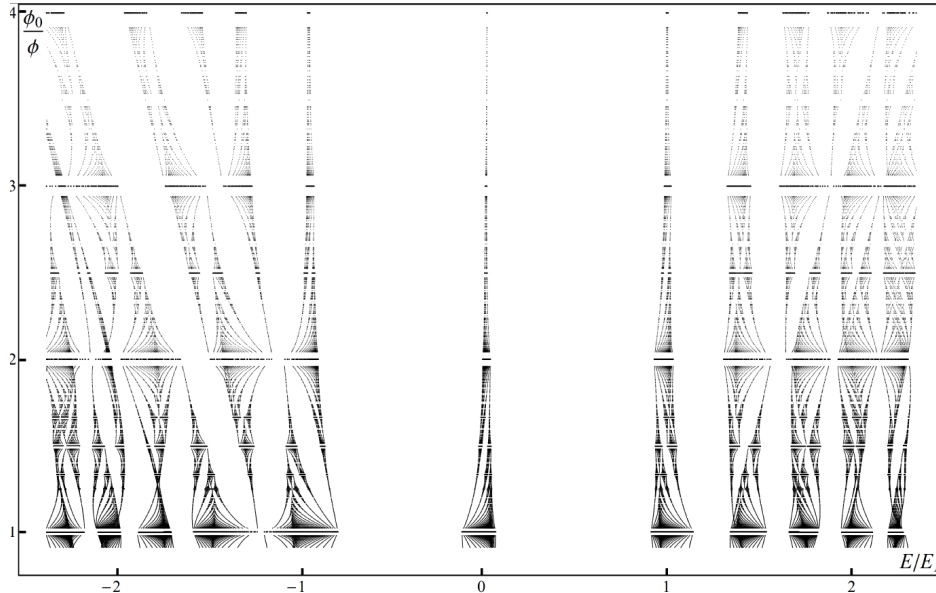

Fig. S10. Hidden periodicity of moiré butterflies. The superlattice spectrum in Fig. 3c of the main text is replotted as a function of ϕ_0/Φ with the energy scale renormalized to E_1. It is the presentation standard for research on semiconductor superlattices [S19-21]. There are obvious Zak's oscillations with the energy gaps tending to close at integer ϕ_0/Φ. There is no obvious periodicity within each Landau band that occurs in semiconductor superlattices [S19-S21]. Nevertheless, notice that the first pattern (ϕ_0/Φ between 1 and 2) within, for example, the 1st LL is similar to the second pattern for the 2nd LL, and so on. This periodicity involving both ϕ_0/Φ and N also survives in part for the hole side of the spectrum where the mixing between different LLs is much stronger.

Supplementary references

[S1] C. Dean *et al*. Graphene based heterostructures. *Solid State Commun.* **152**, 1275-1282 (2012).

[S2] A. S. Mayorov *et al*. Micrometer-scale ballistic transport in encapsulated graphene at room temperature. *Nano Lett.* **11**, 2396-2399 (2011).

[S3] K. S. Novoselov *et al*. Two dimensional gas of massless Dirac fermions in graphene, *Nature* **438**, 197-200 (2005).

[S4] L. A. Ponomarenko *et al.* Tunable metal–insulator transition in double-layer graphene heterostructures. *Nature Physics* **7**, 958-961 (2011).

[S5] A. S. Mayorov *et al*. How close can one approach the Dirac point in graphene experimentally? *Nano Lett.* **12**, 4629-4634 (2012).

[S6] A. S. Mayorov *et al*. Interaction-driven spectrum reconstruction in bilayer graphene. *Science* **333**, 860-863 (2011).

[S7] M. Zarenia, O. Leenaerts, B. Partoens, F. M. Peeters. Substrate-induced chiral states in graphene. *Phys. Rev. B* **86**, 085451 (2012))

[S8] M. M. Kindermann, B. Uchoa, D. L. Miller. Zero energy modes and gate-tunable gap in graphene on hexagonal boron nitride. *Phys. Rev. B* **86**, 115415 (2012).

[S9] M. Yankowitz *et al*. Emergence of superlattice Dirac points in graphene on hexagonal boron nitride. *Nature Phys.* **8**, 382–386 (2012).

[S10] C. Ortix, L. Yang, J. van den Brink. Graphene on incommensurate substrates: Trigonal warping and emerging Dirac cone replicas with halved group velocity. *Phys. Rev. B* **86**, 081405 (2012).

[S11] J. R. Wallbank *et al*. Generic miniband structure of graphene on a hexagonal substrate. arXiv:1211.4711 (2012).

[S12] C. H. Park *et al*. New generation of massless Dirac fermions in graphene under external periodic potentials. *Phys. Rev. Lett.* **101**, 126804 (2008).

[S13] F. Guinea, T. Low. Band structure and gaps of triangular graphene superlattices. *Phil. Trans. Royal Soc. A* **368**, 5391-5402 (2010).

[S14] J. Zak. Magnetic translation group, *Phys. Rev.* **134**, A1602-A1606 & A1607-A1611 (1964).

[S15] E. Lifshitz, L. Pitaevski. *Statistical Physics* –Part 2.

[S16] D. R. Hofstadter. Energy levels and wave functions of Bloch electrons in rational and irrational magnetic fields. *Phys. Rev. B* **14**, 2239-2249 (1976).

[S17] R. Bistritzer, A. MacDonald. Moire butterflies. *Phys. Rev. B* **84**, 035440 (2011).

[S18] J. W. Rhim, K. Park. Self-similar occurrence of massless Dirac particles in graphene under magnetic field. *Phys. Rev. B* **86**, 235411 (2012).

[S19] C. Albrecht *et al*. Evidence of Hofstadter's fractal energy spectrum in the quantized Hall conductance. *Phys. Rev. Lett*. **86**, 147-150 (2001).

[S20] M. C. Geisler *et al*. Detection of a Landau band-coupling-induced rearrangement of the Hofstadter butterfly. *Phys. Rev. Lett*. **92**, 256801 (2004).

[S21] D. Pfannkuche, R.R. Gerhardts. Theory of magnetotransport in two-dimensional electron systems subjected to weak two-dimensional superlattice potentials. *Phys. Rev*. *B* **46**, 12606-12626 (1992).